

Simulation of Alfvénic avalanche onset in NSTX

Cite as: Phys. Plasmas **27**, 022117 (2020); <https://doi.org/10.1063/1.5136236>

Submitted: 11 November 2019 . Accepted: 21 January 2020 . Published Online: 24 February 2020

R. B. White , V. N. Duarte , N. N. Gorelenkov , E. D. Fredrickson , and M. Podesta 



View Online



Export Citation



CrossMark

ARTICLES YOU MAY BE INTERESTED IN

[Mechanisms of energetic-particle transport in magnetically confined plasmas](#)

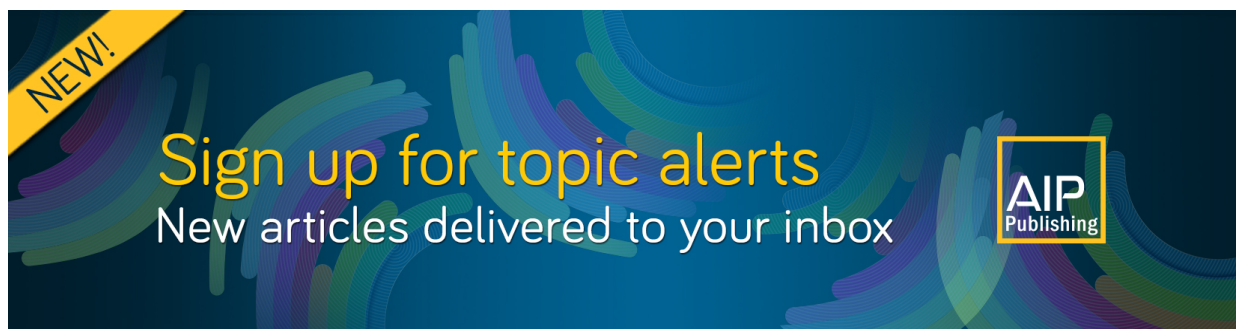
Physics of Plasmas **27**, 030901 (2020); <https://doi.org/10.1063/1.5136237>

[A new explanation of the sawtooth phenomena in tokamaks](#)

Physics of Plasmas **27**, 032509 (2020); <https://doi.org/10.1063/1.5140968>


[Machine learning control for disruption and tearing mode avoidance](#)

Physics of Plasmas **27**, 022501 (2020); <https://doi.org/10.1063/1.5125581>



NEW!

Sign up for topic alerts
New articles delivered to your inbox



Simulation of Alfvénic avalanche onset in NSTX

Cite as: Phys. Plasmas **27**, 022117 (2020); doi: [10.1063/1.5136236](https://doi.org/10.1063/1.5136236)

Submitted: 11 November 2019 · Accepted: 21 January 2020 ·

Published Online: 24 February 2020



View Online



Export Citation



CrossMark

R. B. White,^{a)} V. N. Duarte, N. N. Gorelenkov, E. D. Fredrickson, and M. Podesta

AFFILIATIONS

Princeton Plasma Physics Laboratory, Princeton University, Princeton, New Jersey 08543, USA

^{a)}Electronic mail: rwhite@pppl.gov

ABSTRACT

In some tokamak discharges, a number of Alfvén eigenmodes (AEs) have been observed to cause a large-scale collapse of the high energy particle distribution, a phenomenon referred to as an avalanche. We examine the necessary conditions for an avalanche using the available experimental information from NSTX on the equilibrium and mode properties for two cases, one with a measurable but benign AE activity and one with an AE activity leading up to an avalanche. To produce an avalanche, the modes present in the discharge must possess resonances that can overlap with a modest increase in instability magnitude, providing a path to global particle stochastic motion. We find that the modes present in the avalanche-free discharge do not provide such a path even at a very large amplitude. During the discharge which subsequently produces an avalanche, the high energy population is growing and the Alfvén frequency is dropping due to increasing density, and we find that both these changes, producing a small increased drive or an increased resonance width for the Alfvén modes, can lead in this case to uncontrolled mode growth and large-scale beam particle loss.

Published under license by AIP Publishing. <https://doi.org/10.1063/1.5136236>

I. INTRODUCTION

Alfvén modes can produce significant modification of high energy particle distributions and even cause losses. It is thus important to develop reliable theoretical models to describe mode evolution, saturation, and the effect of the modes on particle distributions. Full-scale calculations of mode evolution require extensive computational efforts. Reliable simpler models that produce similar results are useful for a more rapid understanding of physical phenomena and in promoting the understanding of which details and mechanisms are relevant for the description of events.

Avalanches are sudden and simultaneous amplitude bursts of many Alfvén modes accompanied by the modification of particle distribution, sometimes including induced loss. Avalanches occur frequently in super-Alfvénic neutral beam heated NSTX plasmas¹ and are observed to take place when the fast ion pressure exceeds roughly 30% of the total plasma pressure.² They can be responsible for serious degradation of fast ion confinement, which can reach up to 50% of the fast ions, as inferred from the drop in the neutron rate.^{3,4} Similar explosive events are frequently observed in negative-ion beam heated JT-60U discharges and are referred to as abrupt large events (ALEs).^{5,6} During the avalanches, the modes attain unusually large amplitudes to the point that MHD wave-wave nonlinearities may regulate the system's dynamics. Self-consistent models are able to capture explosive growth due to multiple resonance overlaps, such as the broadening quasilinear approach of Ref. 7, and to capture wave-particle nonlinearities, but assume that linear properties of the modes, such as the

eigenstructure and resonance condition, remain unchanged. This treatment can be sufficient to discover the necessary conditions for the occurrence of the onset of explosive growth.

In this work, we examine weakly unstable damped Alfvén modes present in NSTX,¹ using numerical equilibria and particle distributions, and including the time evolution of the modes observed to be present in the discharges. We consider two discharges, the first involving benign saturated modes, and the second with modes producing an avalanche, using the guiding center code ORBIT⁸ and a δf formalism to reproduce the evolution of the modes. The code uses numerically produced NSTX equilibria, mode eigenfunctions produced by NOVA-K,⁹ and numerical beam particle distributions produced by TRANSP's NUBEAM module,¹⁰ and has been described in previous publications.^{11,12}

In Sec. II, we introduce the necessary mathematical formalism to discuss the time evolution of Alfvén modes in a tokamak. In Sec. III, we simulate modes observed in a discharge to saturate quasi-steadily at benign amplitudes and not produce significant modification of the particle distribution. In Sec. IV, we simulate the amplitude evolution of modes in a NSTX discharge in which an avalanche occurred. In Sec. V, the conclusions are presented.

II. ALFVÉN MODE EVOLUTION

The equilibrium magnetic field is given by

$$\vec{B} = g\nabla\zeta + I\nabla\theta + \delta\nabla\psi_p, \quad (1)$$

where θ and ζ are poloidal and toroidal coordinates and ψ_p is the poloidal flux, and in an axisymmetric equilibrium using Boozer coordinates, g and I are functions of ψ_p only. The perturbation has the form $\delta\vec{B} = \nabla \times \alpha\vec{B}$, and α and an electric potential Φ have the Fourier expansions

$$\alpha = \sum_{m,n} A_n \alpha_{m,n}(\psi_p) \sin(\Omega_{mn}), \quad \Phi = \sum_{m,n} A_n \Phi_{m,n}(\psi_p) \sin(\Omega_{mn}), \quad (2)$$

where n refers to a single mode with a definite toroidal mode number n and frequency ω_n and the sum is over toroidal and poloidal harmonics m with $\Omega_{mn} = n\zeta - m\theta - \omega_n t - \phi_n$, with ϕ_n being the mode phase. For ideal modes, the electric potential Φ is chosen to cancel the parallel electric field induced by $d\vec{B}/dt$, requiring

$$\sum_{m,n} \omega_n B \alpha_{m,n} \cos(\Omega_{mn}) - \vec{B} \cdot \nabla \Phi / B = 0$$

giving in Boozer coordinates

$$(gq + I)\omega_n \alpha_{mn} = (nq - m)\Phi_{mn}.$$

The perturbation α is related to the ideal displacement $\vec{\zeta}$, through¹³

$$\alpha_{mn} = \frac{(m/q - n)}{(mg + nI)} \zeta_{mn}^{\psi}.$$

The eigenfunctions produced with the code NOVA-K are normalized with the largest harmonic $\zeta_{mn}^{\psi}(\psi_p)$ having the maximum amplitude 1. Thus, the amplitude A_n is the magnitude of the ideal displacement caused by this harmonic, normalized to the major radius R , which is 100 cm in this case.

The equations of motion in the Hamiltonian form are^{8,13}

$$\begin{aligned} \dot{\theta} &= \frac{\partial H}{\partial P_\theta}, & \dot{P}_\theta &= -\frac{\partial H}{\partial \theta}, \\ \dot{\zeta} &= \frac{\partial H}{\partial P_\zeta}, & \dot{P}_\zeta &= -\frac{\partial H}{\partial \zeta}, \end{aligned} \quad (3)$$

where canonical momenta are

$$P_\zeta = g\rho_{\parallel} - \psi_p, \quad P_\theta = \psi + \rho_{\parallel} I, \quad (4)$$

and ψ is the toroidal flux, with $d\psi/d\psi_p = q(\psi_p)$, the field line helicity, and $\rho_{\parallel} = v_{\parallel}/B$.

Stepping equations for the mode amplitude and phase were previously derived.^{11,14}

$$\begin{aligned} \frac{dA_n}{dt} &= \frac{-\nu_A^2}{D_n \omega_n A_n} \sum_{j,m} w_{n,j} \left[\rho_{\parallel} B^2 \alpha_{mn}(\psi_p) - \Phi_{mn}(\psi_p) \right] \cos(\Omega_{mn}) \\ &\quad - \gamma_d A_n, \end{aligned} \quad (5)$$

$$\frac{d\phi_n}{dt} = \frac{-\nu_A^2}{D_n \omega_n A_n^2} \sum_{j,m} w_{n,j} \left[\rho_{\parallel} B^2 \alpha_{mn}(\psi_p) - \Phi_{mn}(\psi_p) \right] \sin(\Omega_{mn}), \quad (6)$$

with $D_n = 4\pi^2 \sum_m \int \zeta_{mn}^2(\psi_p) d\psi_p$, j the particle index, and ψ_p, θ, ζ the position and ρ_{\parallel} the normalized parallel velocity of particle j . The modes are resonant with and destabilized by the high energy injected beam, so the particles refer to beam ions. The linear damping rate γ_d is due to the continuum, trapped particle collisional damping, electron

and thermal ion Landau damping, and radiation, all terms in the sums are evaluated at the coordinates of particle j , and $w_{n,j}$ is the δf weight of particle j for mode n .

The perturbed distribution δf is represented by

$$\begin{aligned} \delta f(\psi_p, \theta, \zeta, \rho_{\parallel}, t) &= \sum_j w_{n,j} \delta(\psi_p - \psi_{p,j}(t)) \delta(\theta - \theta_j(t)) \delta(\zeta \\ &\quad - \zeta_j(t)) \delta(\rho_{\parallel} - \rho_{\parallel,j}(t)) \end{aligned} \quad (7)$$

and the particle weights are stepped by

$$\frac{dw_{n,j}}{dt} = \frac{w_{n,j} - f/g}{f_0} \left[\partial_E f_0 \dot{E} + \partial_{P_\zeta} f_0 \dot{P}_\zeta \right] \quad (8)$$

with f being the time dependent beam distribution, g the marker distribution given by $\psi_{p,j}, \theta_j, \zeta_j$ and $\rho_{\parallel,j}$, and f_0 the unperturbed initial beam distribution. The particle energy E and P_ζ are both conserved in time in the absence of the modes. The changes in the time of the particle energy and canonical momentum due to the modes are given by

$$\frac{dE}{dt} = -\rho_{\parallel} B^2 \partial_t \alpha + \partial_t \Phi, \quad \frac{dP_\zeta}{dt} = \rho_{\parallel} B^2 \partial_\zeta \alpha - \partial_\zeta \Phi. \quad (9)$$

The necessary theoretical input to be able to predict Alfvén mode saturation amplitudes consists of a numerical representation of the high energy particle distribution producing the unstable modes, the plasma equilibrium, the mode eigenfunction structure, the values for mode damping, and the rate of particle collisions, which are responsible for the replenishment of the particle density gradient in a resonance. The mode damping is taken to be constant in time. The evolution of the mode can then be followed up to saturation, giving a clear idea of the effect of the mode on the particle distribution.

It is not necessary to use the full beam particle distribution given by TRANSP in these simulations for the calculation of the partial derivatives required for Eq. (8). Doing so is in fact difficult, because of errors introduced in the necessary smoothing. But all energy exchange between modes and particles occurs at the resonances. Particles on good Kolmogorov-Arnold-Moser (KAM)¹⁵ surfaces only exhibit adiabatic oscillations of energy and canonical momentum, and cannot contribute to mode growth. Thus, simulating modes agreeing with theoretical or experimental growth rates require only the numerical imposition of the correct energy and momentum gradients at the locations of the resonances, and not the use of the full particle distribution. The full distribution is however useful as an input for the marker distribution g .

III. QUASI-STEADY STABLE MODE SATURATION

Stable saturated modes were observed in NSTX shot 141655. Other modes are present at a lower frequency, but the two modes selected for analysis are the most stable and best diagnosed. The plasma current was 720 kA, the toroidal field was 3.89 kG, the on axis density was $7 \times 10^{13}/\text{cm}^3$, the beam power was 4.85 MW, and the temperature was 0.9 keV.

Theoretical knowledge of the mode growth rates and damping is unfortunately imprecise, but we can study the possible mode evolution within the boundaries of uncertainty for these values.

The equilibrium and q profile for this shot are shown in Fig. 1. There were two primary modes present, as shown in Fig. 2. Other modes are present at a lower frequency m but they are not very stable

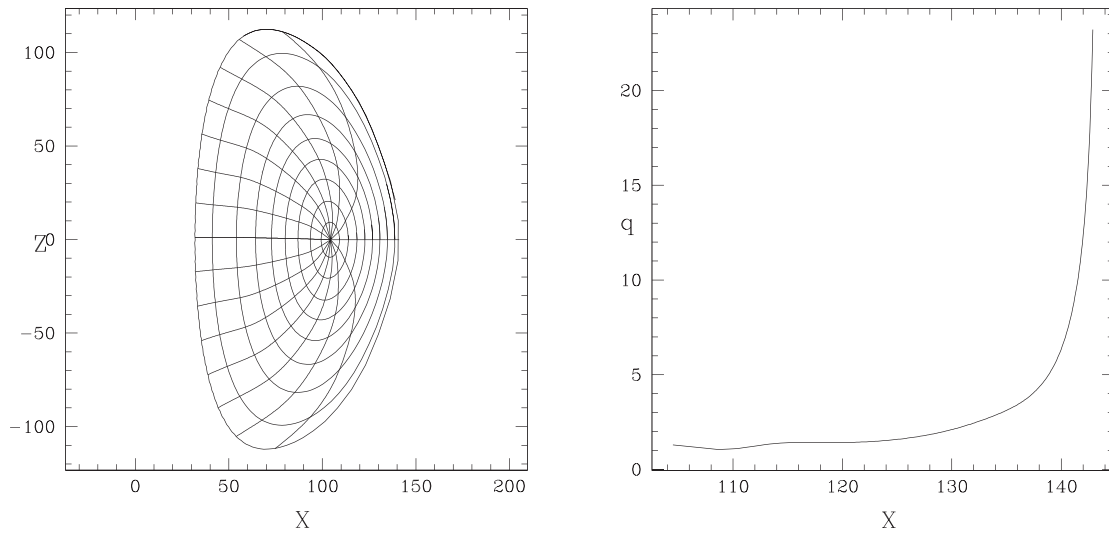


FIG. 1. Equilibrium and q profile for NSTX shot 141655. X and Z are given in cm.

and were poorly diagnosed. An interesting feature of this shot is that two quasi-steady toroidal Alfvén eigenmodes are observed with a nearly constant frequency, in contrast to the more frequent chirping phase in less turbulent scenarios.^{16,17} They were a very steady state and isolated saturated modes, well represented by NOVA-K⁹ The mode amplitudes are shown in Fig. 3, giving ideal displacements of 0.19 mm for $n = 2$ and 0.17 mm for $n = 3$. The amplitudes fluctuate by up to a factor of 2 on sub-millisecond time scales.

In Sec. III, A we introduce the particle distribution given by TRANSP’s NUBEAM module¹⁰ and used in NOVA-K for the calculation of the growth rates and the Alfvén eigenmodes used in the analysis. In Sec. III B, we carry out mode evolution using the δf procedure

and compare with the analytical models for mode saturation and with the experiment.

A. Particle distribution and resonance structure

The energetic particle (EP) distribution function is taken as a product of several factor functions as described recently.¹⁸ They correspond to energy, pitch angle, and canonical momentum dependences shown in Fig. 4 there. The factorized form of the distribution was verified against NUBEAM simulations¹⁹ ORBIT uses variables E , P_ζ , and μ , but the distribution in NOVA-K is given in v , λ , and x , with v being the velocity, $\lambda = v_{\parallel}/v$ the pitch, and $x = \langle \psi / \psi_w \rangle$, where ψ is the

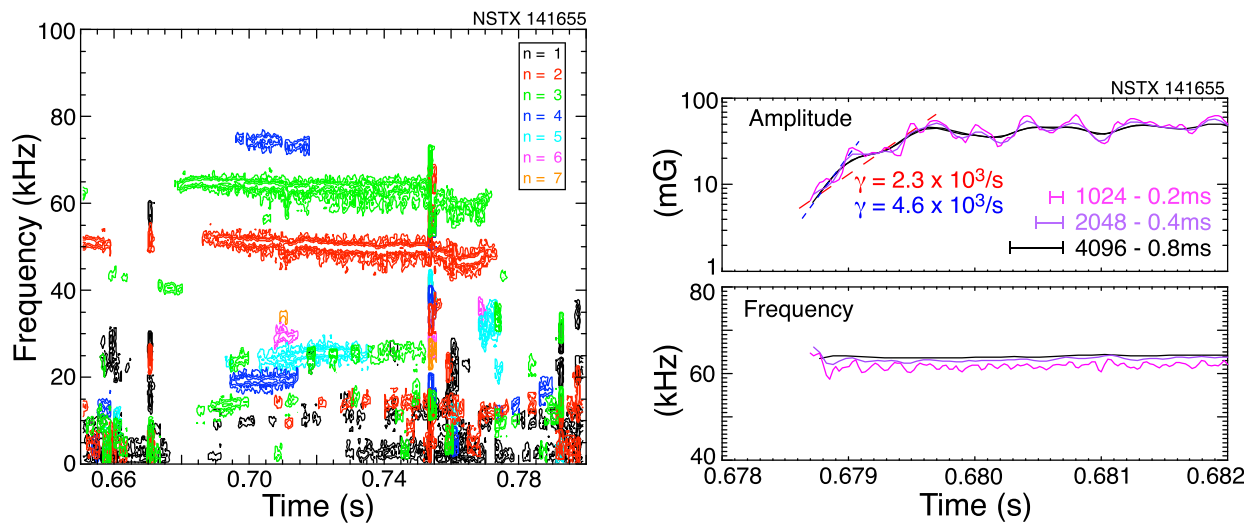


FIG. 2. Observed spectrum and mode evolution in NSTX shot 141655 and growth rate determination for $n = 3$.

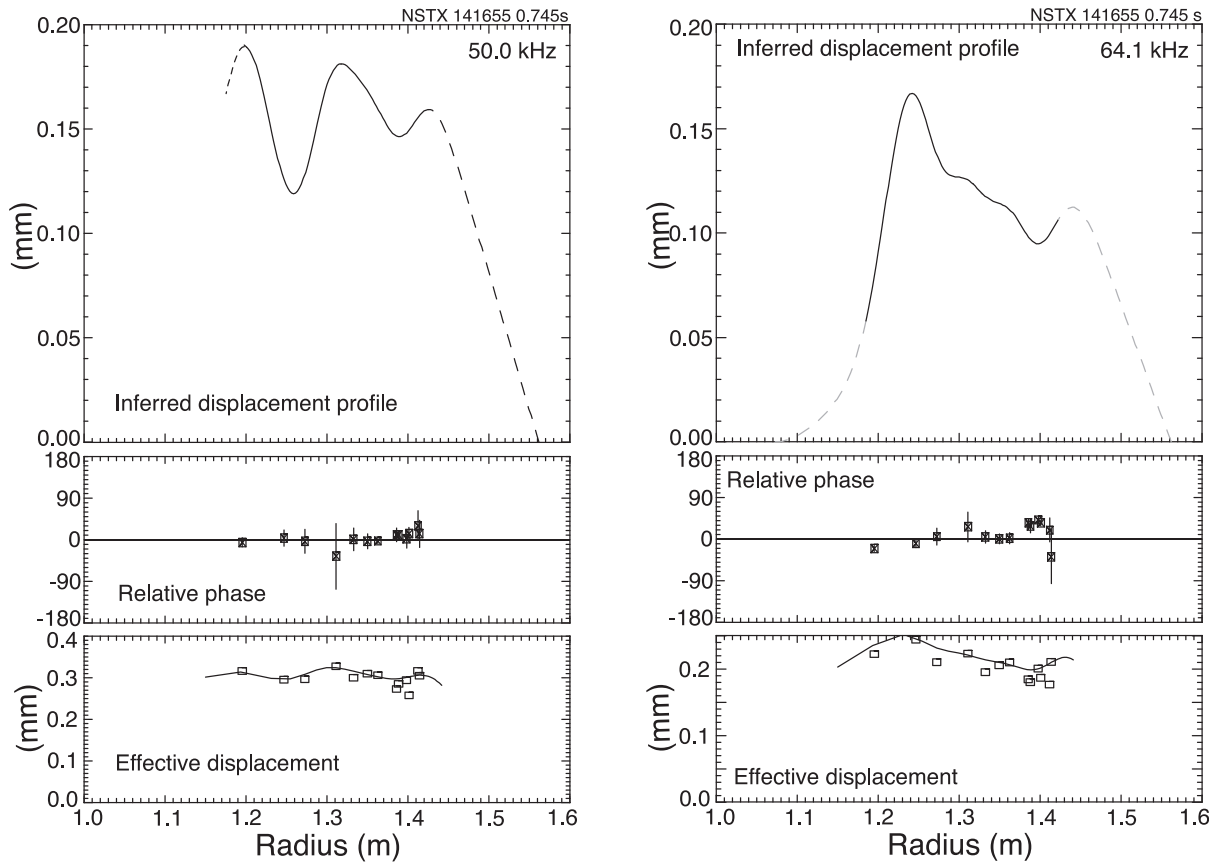


FIG. 3. Experimental determination of mode amplitudes in NSTX shot 141655, $n=2$ (left) and $n=3$ (right), using reflectometer measurements. Simulation of the trial radial displacement profile used to fit reflectometer data. The relative mode phase, within uncertainty, approximately constant with the radius. Simulated reflectometer response profile (solid line) and reflectometer data (points).

toroidal flux, the sub-index w refers to the wall, and the brackets indicate averaging. The distribution is

$$F(v, \lambda, x) = \frac{e^{-(\lambda-\lambda_0)^2/\Delta}}{(v^3 + v_c^3(x))} \sum_0^6 a_n x^n \quad (10)$$

with $a_0 = 0.101754$, $a_1 = 0.0629612$, $a_2 = -2.94924$, $a_3 = 9.95964$, $a_4 = -14.5232$, $a_5 = 10.0517$, $a_6 = -2.70352$, and $\lambda_0 = 0.6$, $\Delta = 0.04$.

$$v_c(x) = 0.07127 \sqrt{\frac{2T_e(x)}{m_e}} \quad (11)$$

and the electron temperature profile is

$$T_e(x) = 0.8788 + 0.0466x - 5.871x^2 + 45.60x^3 - 168.6x^4 + 279.3x^5 - 212.1x^6 + 60.87x^7 \quad (12)$$

in keV. Beam injection is along the midplane, so ion birth is near $\theta = 0$.

The primary drive for Alfvén modes is due to the gradient in the momentum P_ζ , approximately equivalent to a gradient in the minor radius. From Fig. 4, this gradient is approximately $(1/f)\partial_{P_\zeta/\psi_w} f \simeq 30$

(dimensionless) in the outer plasma near $P_\zeta/\psi_w \simeq -0.4$. Near the plasma edge, where the resonances are located, it is approximately half this value. The gradient in the energy variable is weakly stabilizing. Note that the distribution is strongly peaked in the magnetic moment, with μB near 17 keV. The radial displacement of the mode harmonics is shown in Fig. 5, with $3 \leq m \leq 17$, for $n=2$ and with $5 \leq m \leq 34$ for $n=3$. Both modes are located near the plasma edge.

In Fig. 6 are shown kinetic Poincaré plots for amplitudes of $A = 10^{-3}$, for $\mu B = 17$ keV, where the distribution is strongly peaked. “Kinetic” is used to emphasize that these are particle orbits, and not plots of the magnetic field. The plot is only weakly dependent on the value of μ near this value. The primary resonance for the $n=2$ mode is very near the plasma edge, with a smaller resonance at $P_\zeta/\psi_w = 0.2$ with three elliptic points. The resonance near the plasma edge is formed by the contribution of a large number of high m modes, so the distribution of the elliptic points is very irregular. Instead, the internal resonance with 3 elliptic points is dominated by only a few m values, and is more regular. The primary resonance for the $n=3$ mode is at $P_\zeta/\psi_w = 0.08$ with five elliptic points. There is a smaller resonance near the plasma edge.

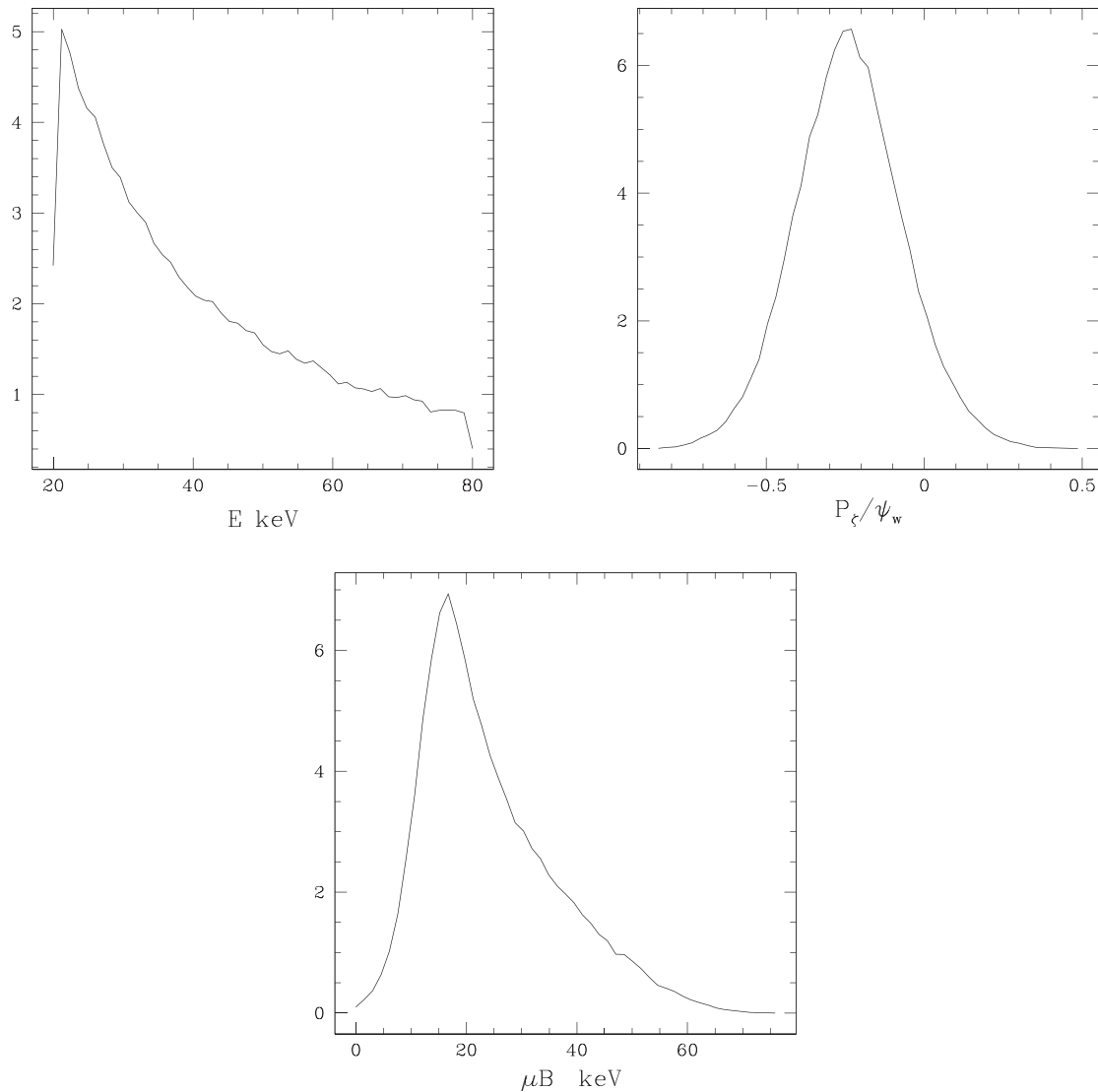


FIG. 4. Particle distribution in E , P_z , and μ_B . Only co-passing particles interact with the resonances.

The 90° pitch-angle scattering collision rate for the dominant resonant particles in this discharge was $\nu_\perp = 2.5/s$, and somewhat smaller near the plasma edge, where the density was lower, the mode frequencies were $f = 45.16$ kHz for $n=2$, and $f = 62.45$ kHz for $n=3$ in the plasma frame at the radial location at the mode maximum, $\psi_p/\psi_w = 0.72$. Strong relative plasma rotation necessitates a transformation from the lab frame to the local plasma frame. The mode is fairly localized, so a single radius for this determination suffices. The ion cyclotron frequency was about 3 MHz, about 50 times the toroidal Alfvén eigenmode (TAE) frequency.

B. Mode evolution

Now, we examine the mode evolution using a δf formalism. We used 100 000 particles, loaded according to the distribution of Sec.

III A. Although the imprecise knowledge of the mode drive and damping values does not allow a precise determination of the saturation values, we find that a large range of drive magnitudes and collision rates produce stable saturation of the two modes. There is no tendency for unlimited mode growth with an induced loss of particles. This is simply understandable due to the fact that the resonances associated with these two modes do not present a path for stochastic particle loss, even when the amplitudes are large.

In Fig. 7 are shown examples of mode evolution from the linear phase up to saturation. The evolution is fit by the analytic expression²⁰ valid near marginal stability

$$A(t) = \frac{A(0)e^{jt}}{\sqrt{1 - b^2(1 - e^{2jt})}}, \quad (13)$$

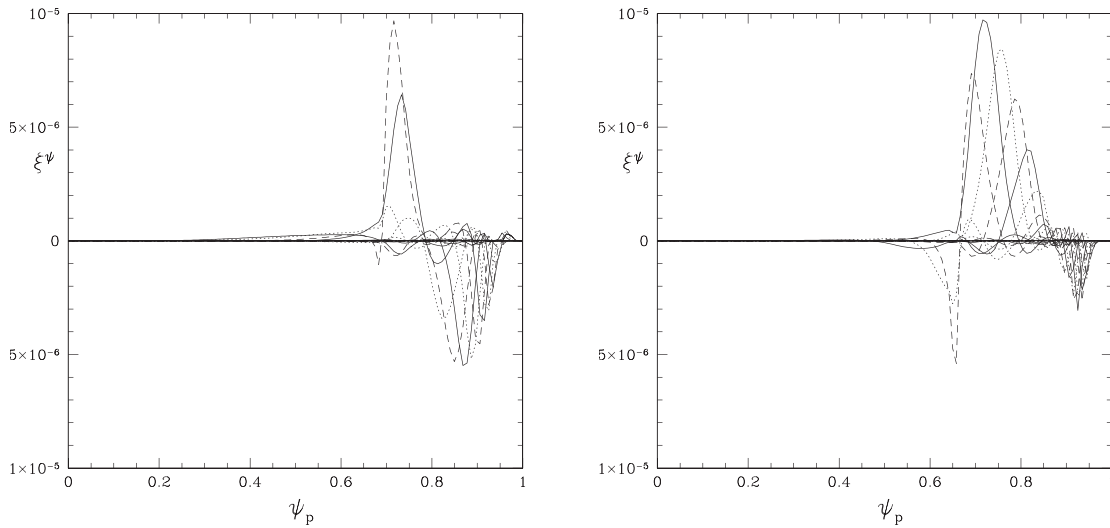


FIG. 5. Mode harmonics $\xi^\psi = \vec{\zeta} \cdot \nabla\psi$, for $n=2$ and $n=3$, amplitude $A = 10^{-5}$. The largest and next largest harmonics for $n=2$ are $m=5$ and $m=6$. The largest and next largest harmonics for $n=3$ are $m=8$ and $m=9$.

with $\gamma = \gamma_L - \gamma_d$, and $b = A(0)/A_{sat}$. γ_L and γ_d are the initial linear growth rate in the absence of damping and the background damping rate of a given mode. $A(0) = 10^{-5}$ was the amplitude at the start of the simulation and A_{sat} is the amplitude saturation level. This fit allows the best determination of the net growth rate, γ , and the saturation level. Even using levels of drive of $(1/f)\partial_{P_\zeta/\psi_w} f = 40$, stronger than those present in the experiment, gives simple saturation with no particle loss.

The growth rate and the saturation amplitude vs drive are shown in Fig. 8. The growth rate for each mode is approximately linear in the drive, as expected. The saturation level, linearly proportional to the growth rate for small amplitudes, scales as the square root of the drive

providing the damping is negligible. The transition between the two regimes might resemble the limitations on the strength of the resonance interaction imposed by radial decoupling and resonance detuning²¹ but in the present simulation, the effect of collisions does not allow for a simple interpretation in terms of that described by Ref. 21. Damping was $\gamma_d/\omega = 0.003$. Experimental values are a displacement of 0.02 cm and 0.017 cm from Fig. 3, or $A = 2 \times 10^{-4}$, 1.7×10^{-4} . This is the best fit with a drive of $(1/f)\partial_{P_\zeta/\psi_w} f \simeq 14$, reasonable for the resonances near the plasma edge. For this small drive, the damping is not negligible and the system is near the instability threshold, a necessary condition for the derivation of Eq. (13). We thus find consistent values of A , $(1/f)\partial_{P_\zeta/\psi_w} f$, and γ for the modes.

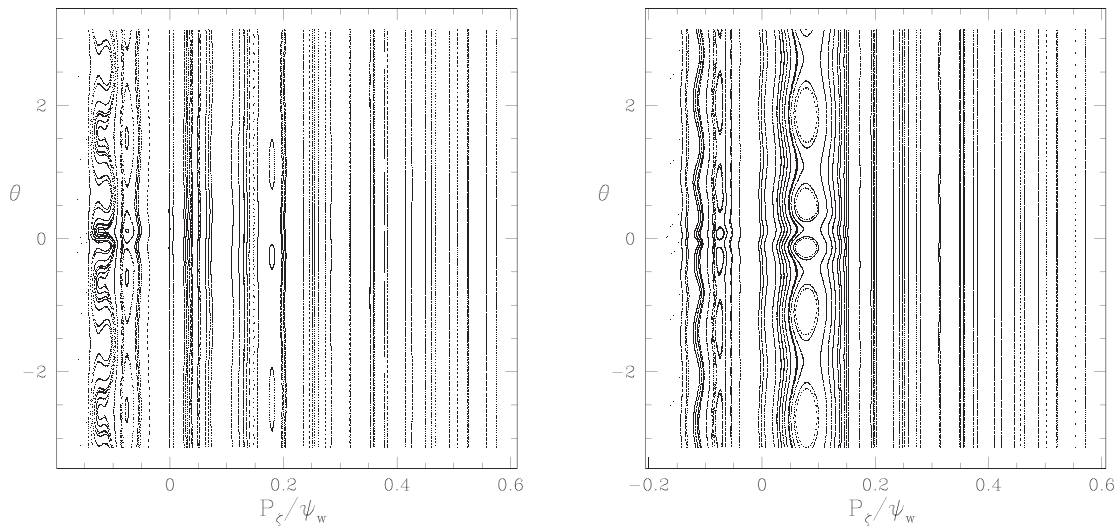


FIG. 6. Kinetic Poincaré plots for the resonances of mode harmonics for $n=2$ and $n=3$, with amplitude $A = 10^{-3}$.

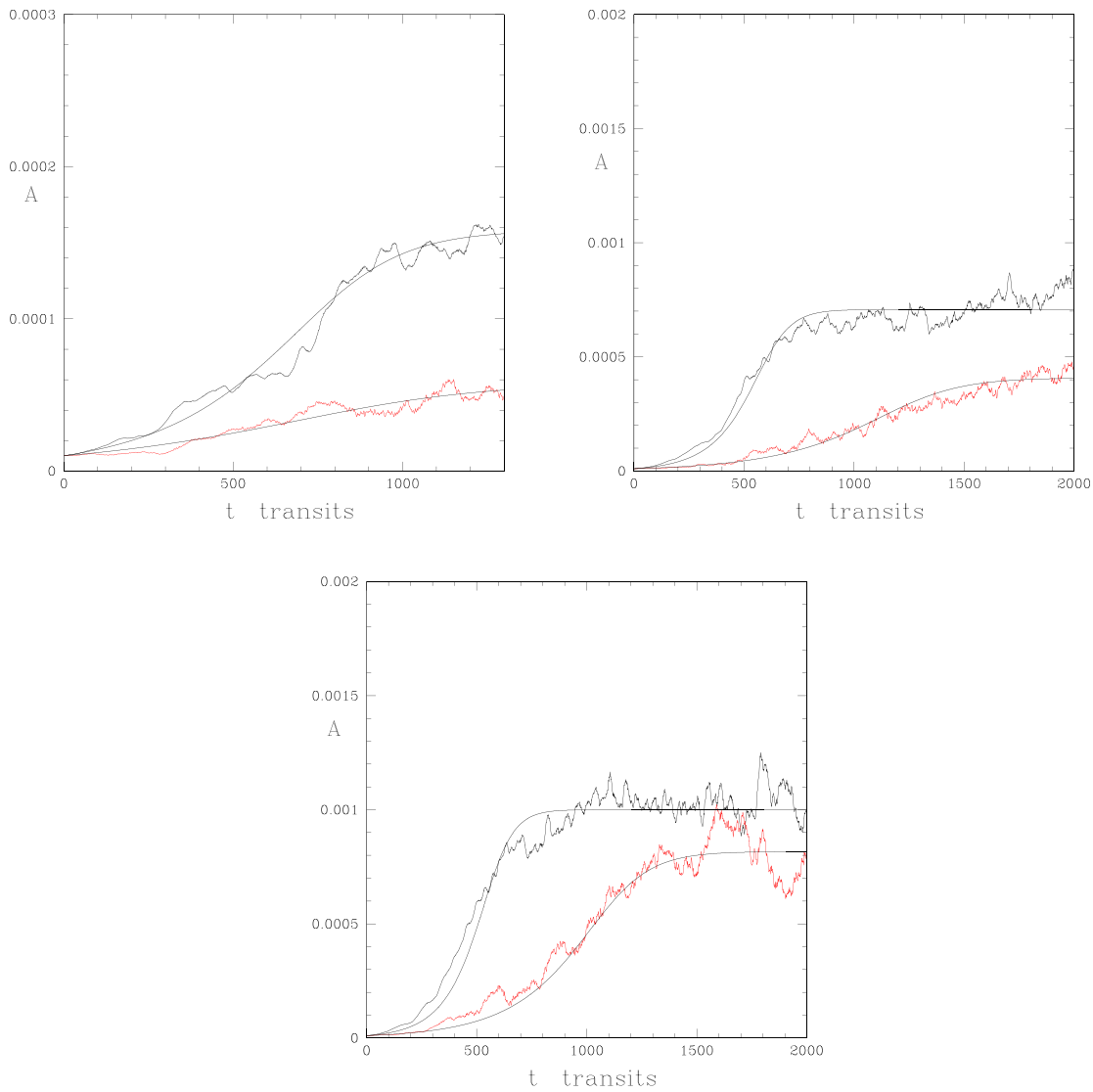


FIG. 7. Mode evolution to saturation, $(1/f)\partial\rho_c/\psi_w f = 12, 20, 25$, $\nu = 2/s$, $n = 3$, (black), and $n = 2$, (red), fit with the theoretical expression given in Eq. (13). The values of γ and A as a function of the drive are shown in Fig. 8. For all cases, $\gamma_d/\omega = 0.003$ and $A(0) = 10^{-5}$.

IV. AVALANCHE SIMULATION

In this section, we consider NSTX shot 141711 at $t = 472$ msec, shortly before the observation of a major avalanche (see spectrogram in Fig. 11). The plasma current was 915 kA, the toroidal field was 4.64 kG, the on axis density was $4.2 \times 10^{13}/\text{cm}^3$, the beam power was 1.9 MW, and the temperature was 1.4 keV. Even though the beam power is significantly less than in the stable case of Sec. III, the Alfvén activity is much stronger. We will see that it is the location and strength of the resonances which are the determining features of the discharge.

The equilibrium and q profile are shown in Fig. 9. The beam particle distribution is shown in Fig. 10, and the distribution in the pitch was strongly peaked near $\mu B = 20\text{keV}$. The modes are destabilized by the gradient in the distribution in P_ζ , approximately equivalent to a

gradient in the minor radius. The gradient in energy E is negative and mildly stabilizing.

There were four primary Alfvén modes present in the discharge before the observed avalanche, with $n = 2, 3, 4, 5$ as well as smaller modes at $n = 1$ and $n = 6$. In Fig. 11 is shown the time history of the mode frequencies leading up to an avalanche crash at around 485 msec. In Fig. 12 is shown the experimental determination of the mode amplitudes for $n = 3, 4, 5$ at $t = 472$ msec, shortly before the avalanche. The $n = 2$ mode was too weak at that time to allow for an accurate determination of amplitude.

Each mode consists of ten or more poloidal harmonics, but only a few of them are large enough to significantly affect the particle distribution through resonance formation. A Poincaré plot showing the

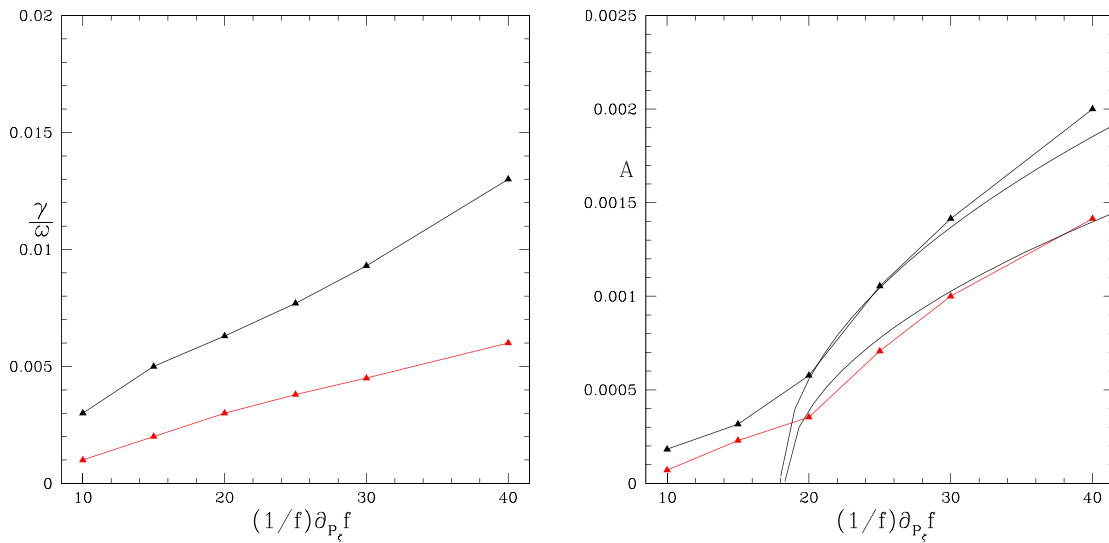


FIG. 8. Growth rate γ/ω with $\gamma = \gamma_L - \gamma_d$ and saturation amplitude, $n=3$ (black) and $n=2$ (red), vs drive $(1/f)\partial_{P_z/\psi_w} f$. The resultant growth rate γ is approximately linear in the value of the drive. The saturation amplitude scales as the square root of the drive provided γ_L is large compared to the damping, and this data is fit with the square root dependence. The $n=3$ mode has $\gamma/\omega \simeq 0.0,028 \pm 0.0,007$.

location of resonances can only be performed for a fixed value of mode frequency and toroidal mode number n , and only gives a limited range of energy. Thus, it is impossible to show the resonances of all modes together over a large energy range using this method. However, one can show the location of the destroyed KAM surfaces^{15,22,23} for all modes together, giving the location of all resonances over a large range of energy. In Fig. 13 is shown the domain of destroyed KAM surfaces for all modes, with the amplitudes fixed at $A = 3 \times 10^{-4}$. The domain in energy E and canonical momentum P_z is that of co-passing ions. The right boundary is the magnetic axis and the left boundary is the plasma edge. All resonances are in the outer half of the plasma, and

extend from 40 keV up to the maximum energy in the beam, about 90 keV. The resonances are far from overlapping at this amplitude, and only produce local flattening of the particle distribution.

The method of destroyed KAM surfaces shows the location of the resonances, but we also wish to associate each individual resonance with the mode responsible for it. For this, we perform kinetic Poincaré plots for each mode separately, showing also the location and number of elliptic points in the poloidal plane.

Kinetic Poincaré plots can be made only with fixed ω and μB . In Figs. 14 and 15 are shown the poloidal harmonics and the resonances for each of the four modes. The resonances are shown for a value of

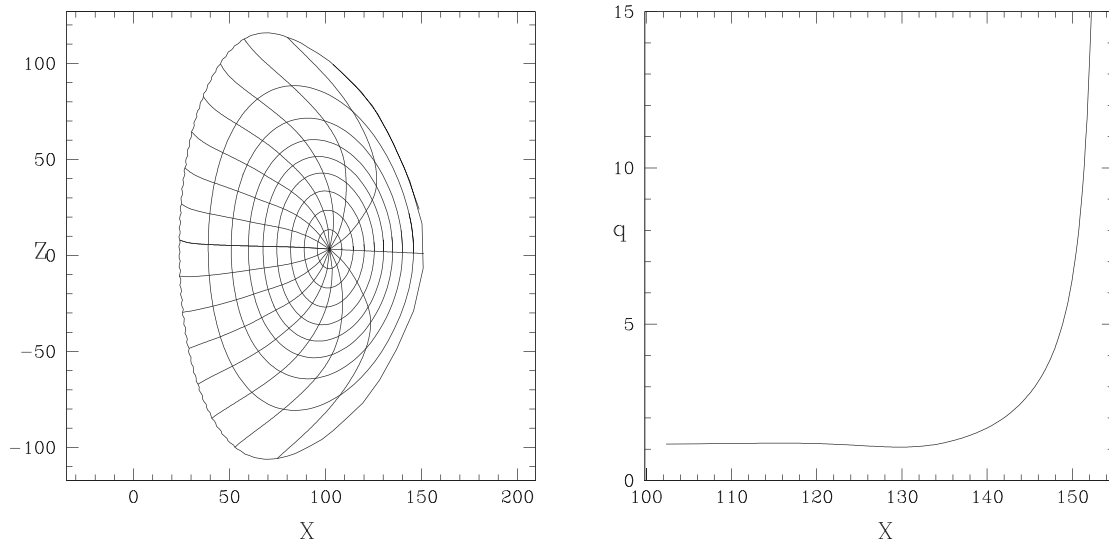


FIG. 9. NSTX shot 141711 at $t = 472$ msec, showing the equilibrium flux surfaces and the q profile. The field on axis was 5.1 kG.

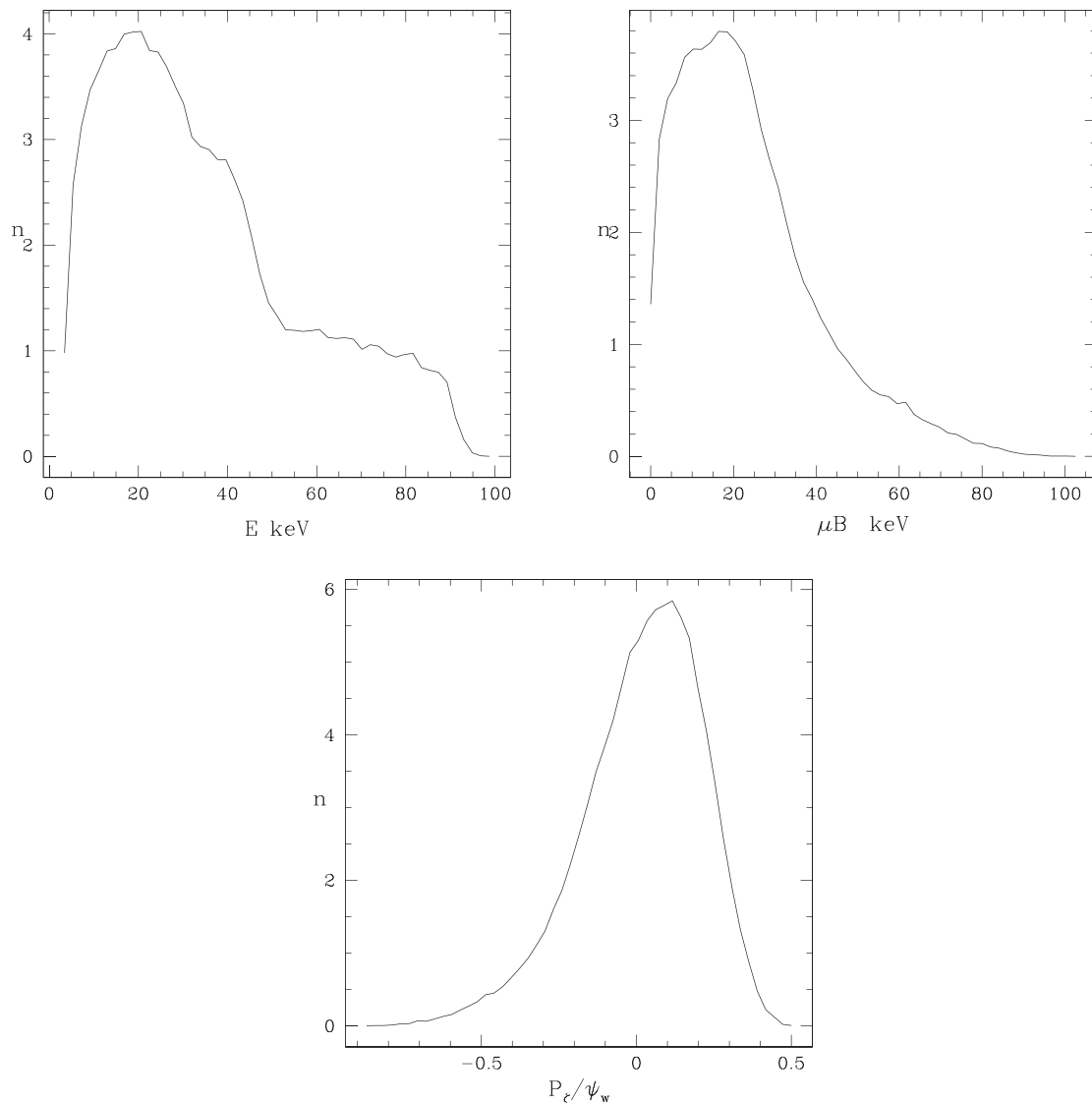


FIG. 10. NSTX shot 141711 beam particle distribution at $t=472$ msec, energy, magnetic moment, and canonical momentum distributions. Only co-passing particles interact with the resonances.

$\mu B = 20\text{keV}$, characteristic of the high energy particle distribution. The location and nature of the resonances is only weakly dependent on this value. For clarity, the resonances are shown in the variable P_ζ , the toroidal canonical momentum, for a large mode amplitude, of $A = 1.5 \times 10^{-3}$. It is interesting that the number of poloidal elliptic points for the major resonance in each case is equal to the n value. Modes with $n=2, 3, 4$ display mostly good KAM surfaces except for the one significant resonance near $P_\zeta/\psi_w = -0.05$. The $n=2$ mode has a smaller resonance at $P_\zeta/\psi_w = -0.37$. The $n=3$ mode has two small resonances at $P_\zeta/\psi_w = -0.3$ and -0.4 . The $n=4$ mode has two small resonances at $P_\zeta/\psi_w = -0.24$ and -0.35 . The mode with $n=5$, in addition to the major resonance at $P_\zeta/\psi_w = -0.05$ has other significant resonances at lower values of P_ζ/ψ_w . The primary

resonance has five elliptic points in the poloidal plane, but there are also resonances with six, seven, and eight elliptic points, and one can also see higher order Fibonacci resonances, one in between the five and six with 11 elliptic points, one in between the six and seven with 13 elliptic points, and one in between the seven and eight with 15 elliptic points. In addition to these higher-order resonances, the coupling of the modes with different n values will produce more. Hence with larger mode amplitude, these resonances can possibly provide a loss channel to the plasma edge, to the left in these plots, at about $P_\zeta/\psi_w = -0.5$.

For a mode of a given toroidal mode number n and frequency ω , the particle energy E and momentum P_ζ are related in the presence of the mode through

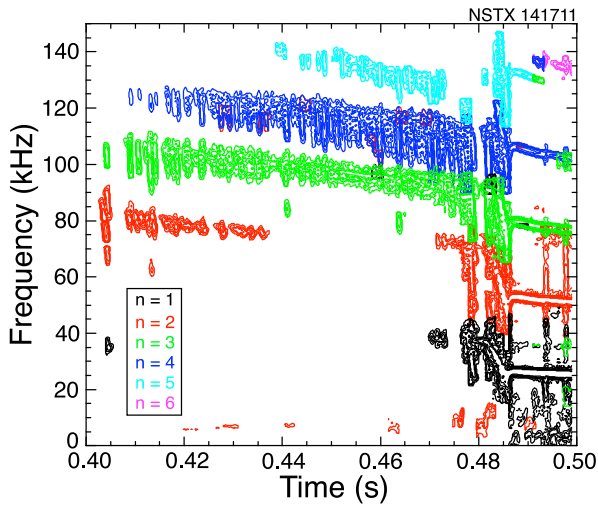


FIG. 11. NSTX shot 141711 modes with $n = 2, 3, 4,$ and 5 leading to an avalanche at $t = 0.485s$.

$$\omega P_{\zeta} - nE = K, \quad (14)$$

with K being a constant depending on the initial particle conditions. The energy range for the data in Figs. 14 and 15 is from 70 to 80 keV.

The domain of the numerical particle distribution in the simulations is chosen to well include all resonances at a large mode amplitude, as well as a full radial distribution, in order to be able to describe to the full extent the discharge conditions leading to an avalanche.

In Table I are shown the growth rates obtained for the mode from the kick model (γ_K).²⁴ Also shown are the theoretically calculated values of the damping for each mode, (γ_d). Although the $n = 2$ mode is stable, the resonances for the modes with $n = 3, 4, 5$ are located directly above the $n = 2$ resonance in P_{ζ} , and thus they naturally steepen the density gradient for the $n = 2$ mode, destabilizing it provided they become large enough.

It is not practical to use the full high energy particle distribution to find the drive for modes because of the numerical difficulty involved in taking partial derivatives in energy and canonical momentum. Instead, we adjust the drive to produce the growth rates determined from the kick model, which does not require derivatives of the distribution for its determination.

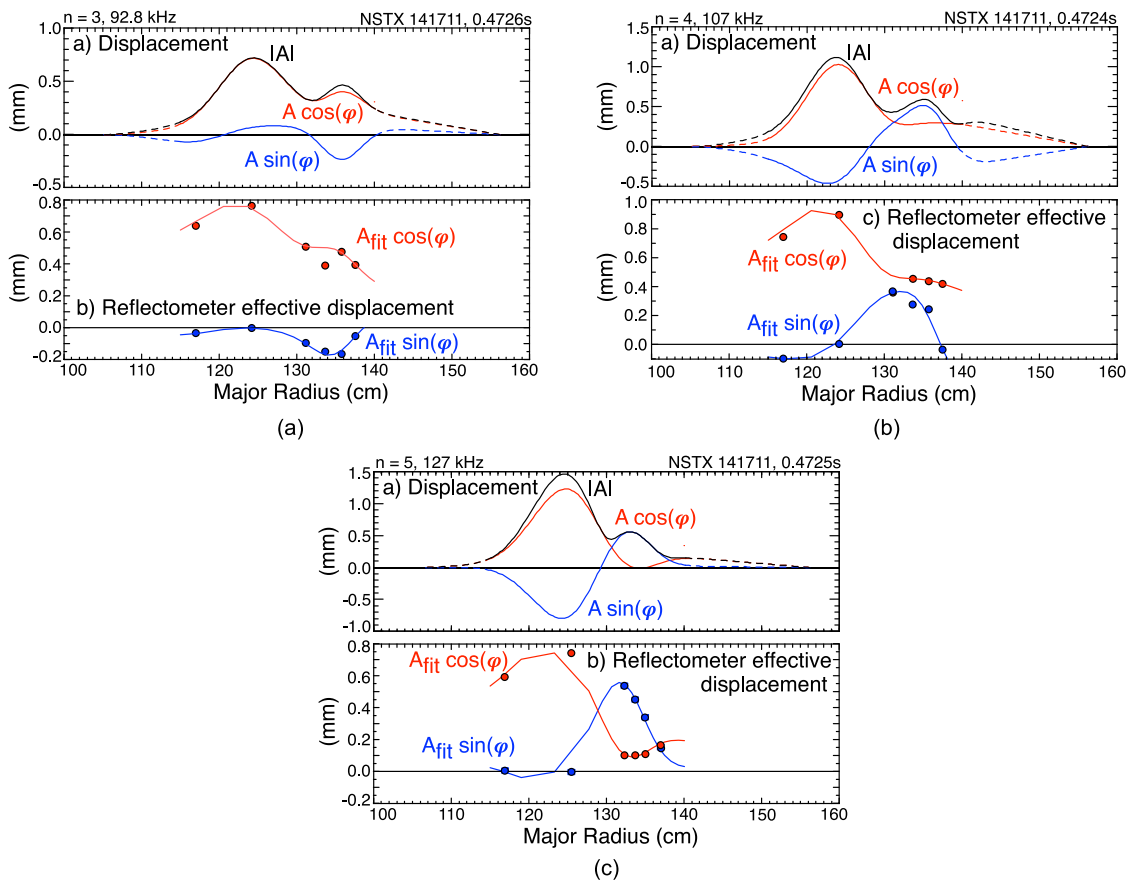


FIG. 12. NSTX shot 141711. Determination of mode displacements at $t = 472$ msec, shortly before the avalanche. (a) Shows the trial sin/cos components of the radial displacement profiles used to fit the reflectometer data. (b) Shows the reflectometer data converted to an effective displacement, which includes interferometer contributions, (circles), and the simulated reflectometer response using the trial functions in (a), solid lines. $n = 3, 0.07$ cm, $n = 4, 0.12$ cm, and $n = 5, 0.14$ cm.

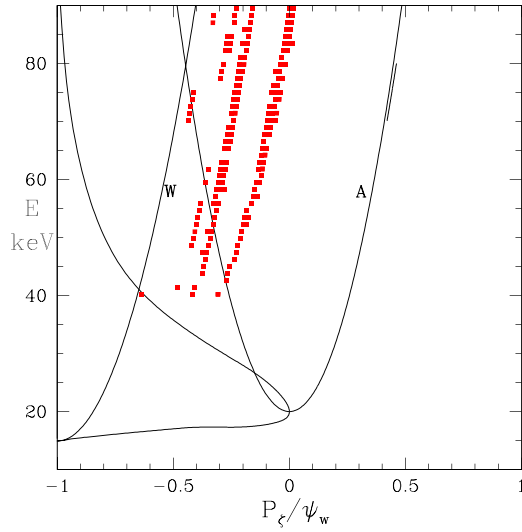


FIG. 13. Resonance location for all modes, $\mu B = 20\text{keV}$ and $A = 3 \times 10^{-4}$. The large domain in the upper right of the diagram is that of co-passing particles. The right edge of this domain is the magnetic axis (A), and the left edge is the plasma boundary (W).

The primary input for the kick model is a set of transport probability matrices that condense the effects of instabilities on energetic particle (EP) dynamics. Matrices are defined over the constant of motion variables E , P_ζ , and μ , which represent the energetic particle energy, canonical toroidal angular momentum, and magnetic moment.^{13,22} For each (E, P_ζ, μ) region in phase space, the matrix contains a probability $p(\Delta E, \Delta P_\zeta)$ of correlated fast ion energy and P_ζ changes (or *kicks*) caused by the instabilities.

The transport matrix is computed via particle-following codes such as the Hamiltonian guiding-center code ORBIT.⁸ For Alfvénic modes that can feature a large number of poloidal harmonics and a complex radial mode structure, mode structures are computed through MHD codes such as NOVA/NOVA-K.^{9,25} To compute a kick probability matrix in ORBIT, the EP phase space is divided into discrete bins to group particles with similar phase space coordinates. Typical numbers of bins for the E , P_ζ , and μ are $n_E \sim 10 - 15$, $n_{P_\zeta} \sim 30 - 40$, and $n_\mu \sim 14 - 20$, respectively. The evolution of (E, P_ζ, μ) of each particle is recorded in ORBIT during the simulation at sampling intervals δt_{samp} . The value of δt_{samp} is chosen to be larger than the period of the instability to filter out fast oscillations and mostly retain changes over the longer time scales associated with particles being trapped in a resonance. For a mode interacting with a fast particle population, the time evolution of the mode energy, E_w , can be expressed as

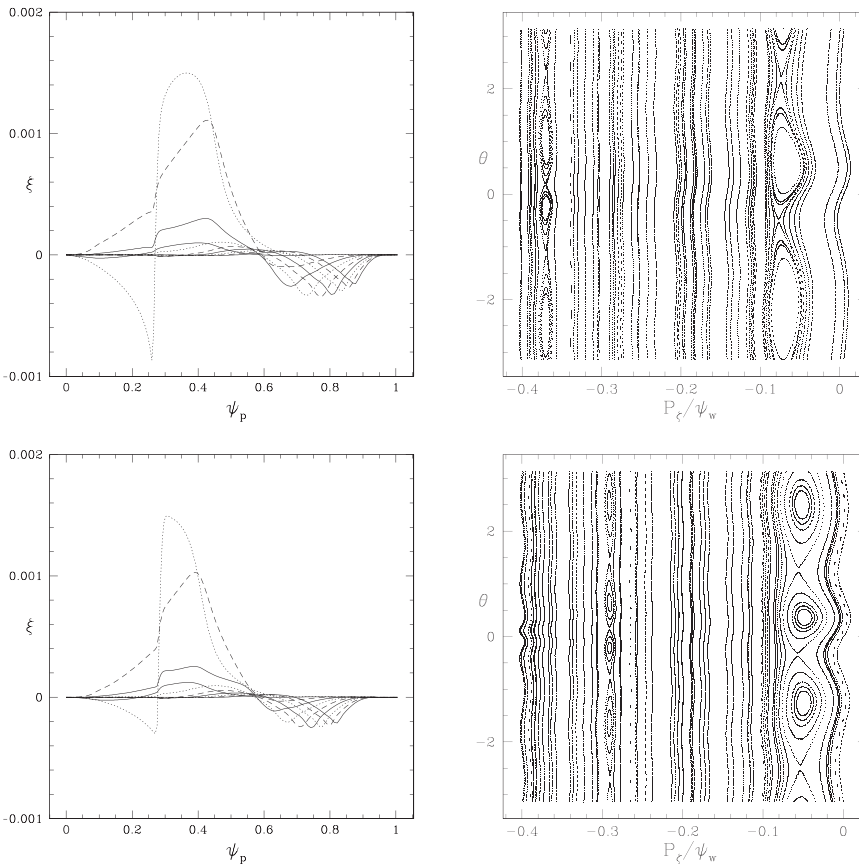


FIG. 14. Eigenstructures and kinetic Poincaré plots for the resonances. Above: Mode $n=2$, $m=1-10$, $\mu B = 20\text{keV}$, and $f = 88.362\text{kHz}$. Below: Mode $n=3$, $m=1-10$, $\mu B = 20\text{keV}$, and $f = 109.507\text{kHz}$. The amplitude (fluid displacement normalized by the major radius) is $A = 2 \times 10^{-3}$ to clearly show the resonance. The largest and next largest harmonics for $n=2$ are $m=2$ and $m=3$. The largest and next largest harmonics for $n=3$ are $m=3$ and $m=4$.

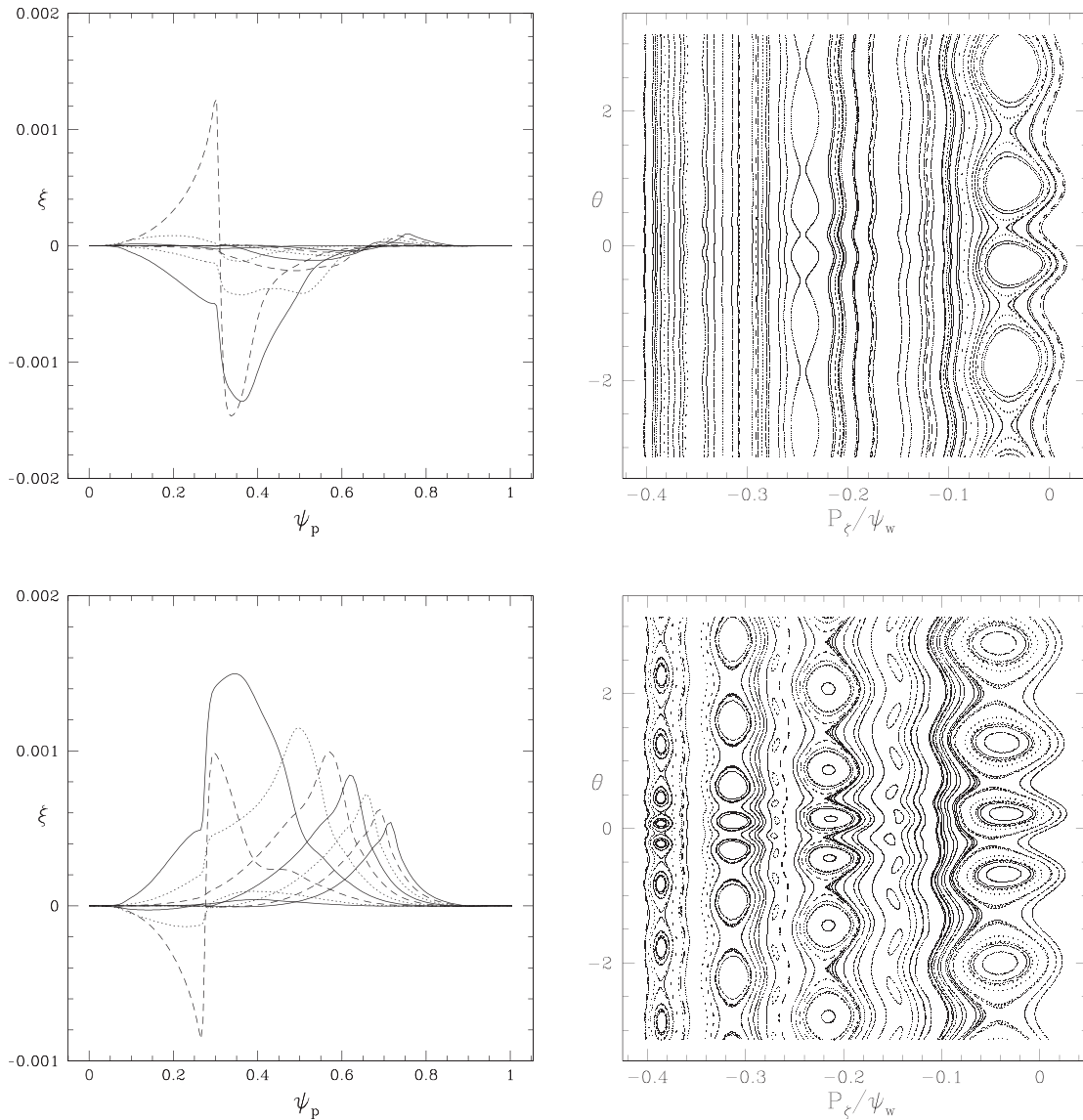


FIG. 15. Eigenstructures and kinetic Poincaré plots for the resonances. Above: Mode $n=4$, $m=1-10$, $\mu B=20$ keV, and $f=126.758$ kHz. Below: Mode $n=5$, $m=1-10$, $\mu B=20$ keV, and $f=161.635$ kHz. The amplitude (fluid displacement normalized by the major radius) is $A=2 \times 10^{-3}$ to clearly show the resonance. The largest and next largest harmonics for $n=4$ are $m=4$ and $m=5$. The largest and next largest harmonics for $n=5$ are $m=6$ and $m=7$.

$$\frac{\partial E_w}{\partial t} = P_{EP} - 2\gamma_{damp} E_w. \quad (15)$$

Here, $P_{EP} = P_{EP}(E_w)$ is the power flowing from the fast ions to the mode and γ_{damp} is the mode's damping rate computed through the NOVA-K code. A growth rate, γ_{gr} , can be introduced in Eq. (15)

$$\gamma_{gr}(E_w) \equiv \frac{P_{EP}(E_w)}{2E_w} \Rightarrow \frac{\partial E_w}{\partial t} = 2[\gamma_{gr} - \gamma_{damp}] E_w. \quad (16)$$

Because of its dependence on the power exchanged between fast ions and the mode(s), the growth rate γ_{gr} is, in general, a function of the instantaneous mode amplitude A_{mode} (proportional to $\sqrt{E_w}$).

TABLE I. Frequency, growth rate, and damping rate corresponding to several toroidal mode numbers.

n	f/kHz	γ_K/ω	γ_d/ω
2	88.4	1.8×10^{-3}	2.85×10^{-3}
3	109.5	8.9×10^{-3}	3.36×10^{-3}
4	126.8	14.5×10^{-3}	1.91×10^{-3}
5	161.6	9.4×10^{-3}	7.5×10^{-4}

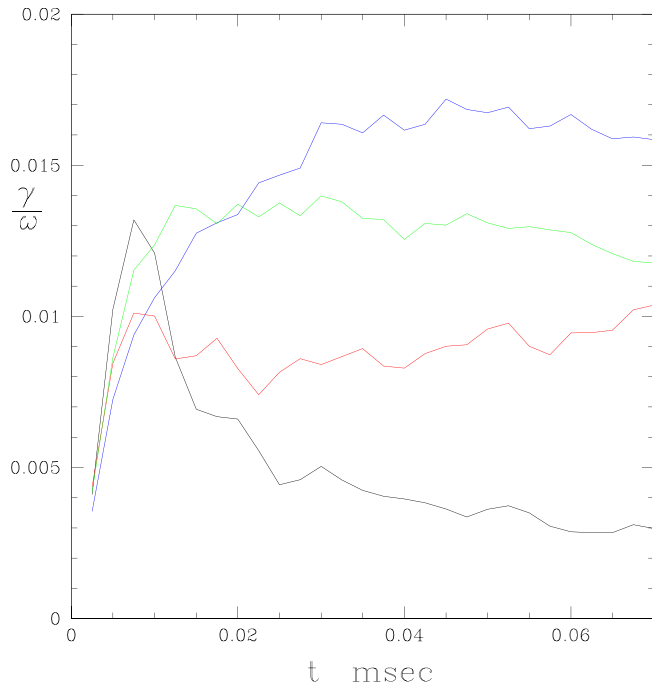


FIG. 16. Numerically determined growth rates from Eq. (5), modes with $n=2$ (black), $n=3$ (red), $n=4$ (blue), and $n=5$ (green).

However, at a sufficiently small mode amplitude, the effect of the mode(s) on the fast ion distribution is negligible. This low-amplitude regime is here referred to as the *linear* phase of mode growth, and can be characterized by a *linear* growth rate

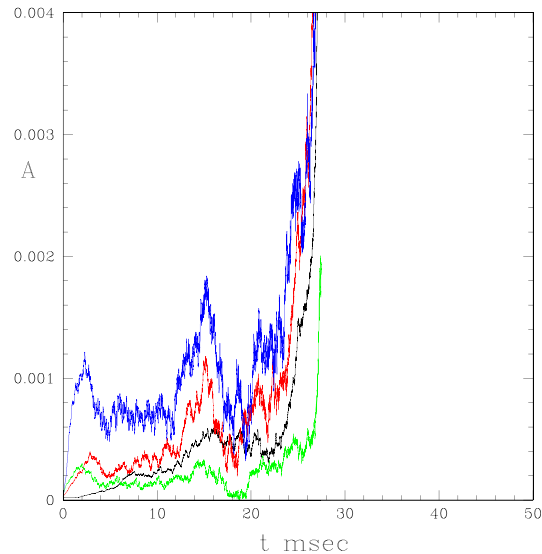
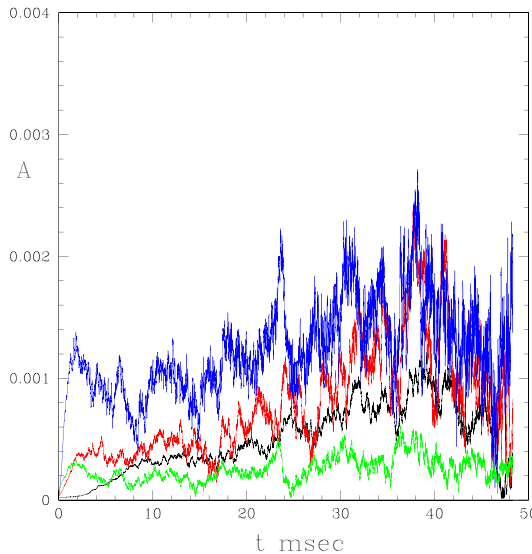


FIG. 17. Mode evolution, modes with $n=2$ (black), $n=3$ (red), $n=4$ (blue), and $n=5$ (green), with a collision frequency of $\nu = 2/s$, for 50 msec. Evolution with normal drive (left) and a 10% increase in drive at 12 msec (right). With the growth rates shown in Fig. 16, the modes fluctuate with amplitudes mostly below 10^{-3} , but with a 10% increase in the drive, there is an explosive growth of all modes, indicating that a δf approach fails to describe the system's dynamics at that point and that wave-wave nonlinearities are likely important.

$$\gamma_{lin} \doteq \lim_{E_w \rightarrow 0} \frac{P_{EP}(E_w)}{2E_w}. \quad (17)$$

Assuming the damping rate and the wave energy E_w are known, for example based on the NOVA/NOVA-K results, Eq. (17) can be used to estimate the linear growth rate from a TRANSP/kick model run that provides P_{EP} .

Directly using Eqs. (5) and (6) for a given value of $(1/f)\partial_{p_c/\psi} f$ also produces a value for γ , which is compared with the kick model results of Table I. The results of the simulation are shown in Fig. 16 giving the growth rates for the modes. This plot was obtained by keeping the mode amplitude fixed at $A = 10^{-5}$, but allowing the particle weights to generate the growth rates. The plot shows the modes with $n=2$ (black), $n=3$ (red), $n=4$ (blue), and $n=5$ (green), with γ/ω less than 0.02 for all modes. The pitch angle scattering rate for the simulations was fixed at the theoretical value of $2/s$ for the observed plasma density. Growth rates are approximately the values given by the kick model.

In Fig. 17 is shown the time evolution of these modes for a period of 50 msec, with a characteristic edge value collision frequency of $2/s$, at the normal drive magnitude and in the simulation in which the drive is made 10% higher at $t = 12$ msec. Both simulations included the theoretical damping values. The plots show the modes with $n=2$ (black), $n=3$ (red), $n=4$ (blue), and $n=5$ (green). For the normal drive, the modes exhibit significant fluctuations but the amplitudes remain mostly below $A = 10^{-3}$. The $n=2$ mode, although initially stable, is slowly destabilized by the other modes, but the amplitude remains below $A = 10^{-3}$. Note that the $n=5$ mode, the only one with resonances extending toward the plasma edge, remains at a low amplitude. In terms of ideal displacement the mode amplitudes are approximately (averaging between 20 and 30 msec) ($n=2$) 0.04 cm, ($n=3$) 0.06 cm, ($n=4$) 0.11 cm, and ($n=5$) 0.03 cm. These agree well with the experimental values shown in Fig. 12 except for $n=5$, for which

the simulation result is too small. However, this mode is strongly modified by the $n = 3$ and $n = 4$ modes, which have stronger growth rates and have resonances intersecting the $n = 5$ resonance, strongly influencing its evolution. The $n = 2$ mode was too small for an accurate experimental determination. As seen, this mode is initially stable, and only destabilized by the action of the other modes.

The explosive solutions in Fig. 17 signal that the δf approach breaks down. They, however, indicate that the increased drive leads to a route of a harder nonlinear scenario in which amplitudes are so large that MHD nonlinearities become relevant and the modes can no longer be treated independently. This observation is somewhat analogous to the breakdown of the nonlinear theory of a discrete mode driven just above the instability threshold developed by Berk *et al.*²⁶ In that case, the occurrence of solutions of a delay integrodifferential equation for mode amplitude blowing up in a finite time were observed to correlate with the formation of phase space structures and the onset of frequency chirping, when compared to full Vlasov simulations.^{16,27} In the Berk-Breizman model, the explosion of solutions indicate that the assumption of a small parameter in the perturbation theory fails to be met, while signaling the tendency for the system evolution to a more pronounced nonlinear phase. The nonlinear chirping has also been numerically simulated²⁸ but a full theoretical understanding of the late nonlinear development of a chirp is still not available. In the present work, we do not attempt to model the amplitude crash. We note, however, that this sort of nonlinear simulation, including the coupling with resistive modes, has been carried out using the code MEGA.^{29–31}

The simplest example of an avalanche is given by the sandpile model.^{32,33} Addition of sand to one part of the sandpile can lead to a cascade of particles in that region, causing an increase in the density gradient in the nearby domains, both above and below this point, and stimulating additional particle flow down the gradient, the effect being thus nonlocal. A similar phenomenon is observed in the present case. Growth of the $n = 3, 4, 5$ modes causes a

change in the gradient of the particle density in the vicinity of the $n = 2$ mode resonance, which was initially stable due to the large damping rate. If the drive is not too large, the modes all stabilize and fluctuate with the amplitudes below the critical values producing a large scale resonance overlap. Experimentally, there is a marked threshold in the large-scale excitation since the onset of avalanches has only been observed to occur when the pressure of fast ions is at least 30% of the total pressure.²

With a 10% increase in drive, these modes grow to a magnitude allowing strong destabilization of the $n = 2$ mode. Additional destabilization of the $n = 5$ mode, the only one with resonances located closer to the plasma boundary and the appearance of significant higher-order Fibonacci sequence resonances (see Fig. 15), leads to a path for particle flux to the plasma edge. The particle evolution cannot be followed during the whole event in these simulations because the modification of the distribution quickly exceeds the limits of the δf formalism, but it is clear that large scale particle loss is likely involved. It is also possible that the particle loss lowers the gradients driving the modes, stabilizing them and halting the flow of particles to the plasma edge before total loss occurs. It is not possible to distinguish these two cases with a δf simulation. In the experiment, the high energy distribution underwent a 20% loss in neutron emission, partly due to particles transferring energy to the modes, decreasing reactivity, and also indicating density profile modification, stabilizing the modes, and then the discharge being recovered.

In Fig. 18 are shown the stochastic domains produced for the final mode amplitudes in the simulations in the two cases. With the drive set to produce the nominal growth rates, only isolated domains of broken KAM surfaces are present, corresponding to the resonances of the modes. The modes do not overlap; there are large domains of good KAM surfaces preventing significant particle loss. If the drive is increased by 10%, the resonances overlap, producing a continuous stochastic domain leading to global particle loss.

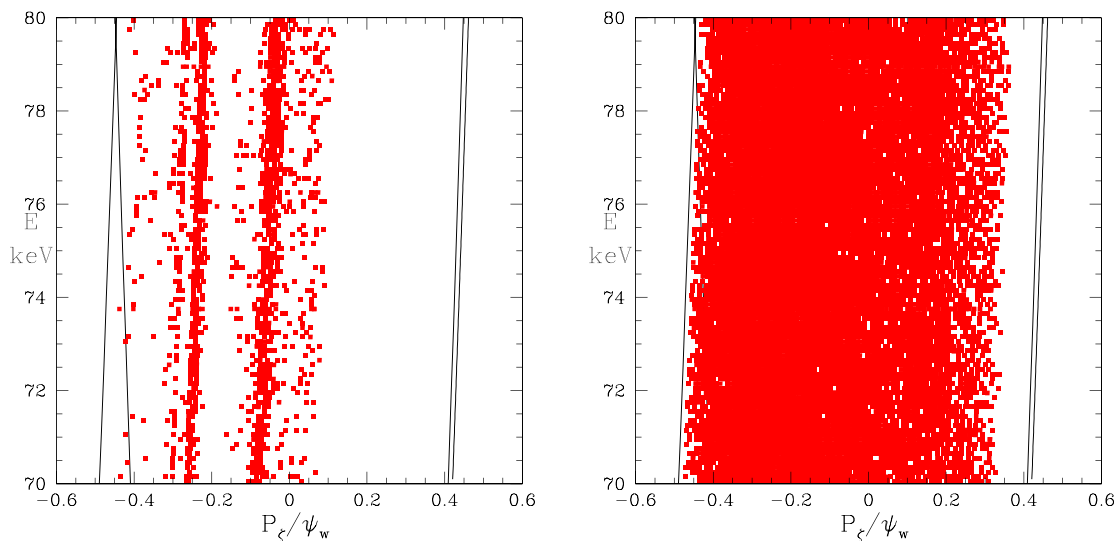


FIG. 18. Domain with broken KAM surfaces for the mode amplitudes observed with the drive producing baseline growth rates, (left) and with the drive multiplied by 1.1 (right). With the normal drive, there are good KAM surfaces preventing significant loss, allowing only local flattening of the distribution, but a 10% increase in the drive leads to global stochastic loss.

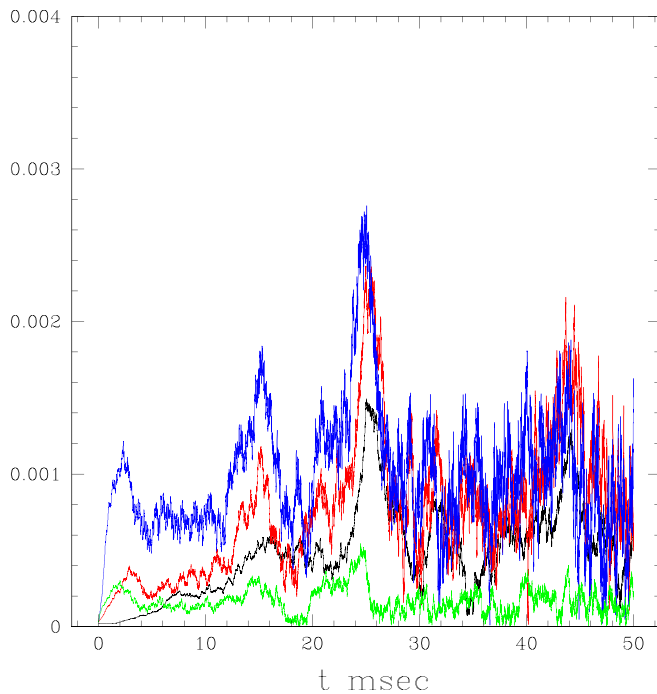


FIG. 19. NSTX shot 141711. Avalanche avoidance by a small increase in the damping of mode $n = 5$ at $t = 25$ msec.

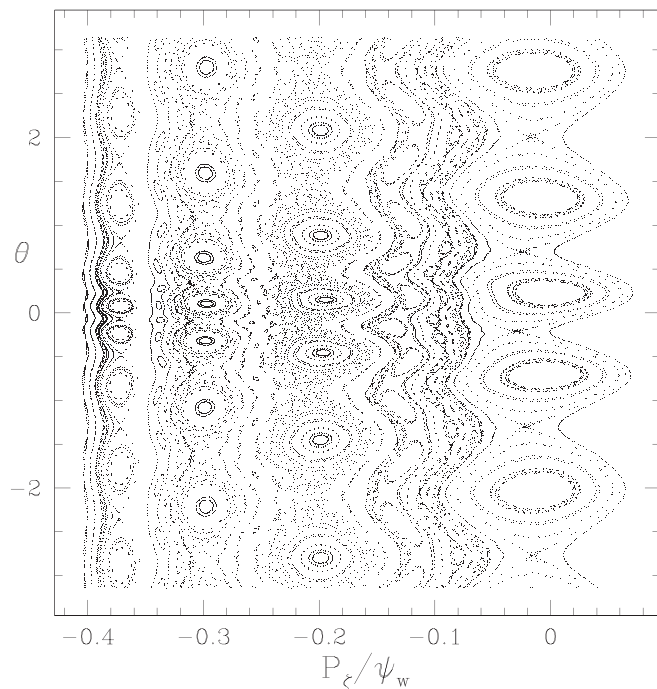


FIG. 20. The kinetic Poincaré plot for the $n = 5$ mode, with the same amplitude as in Fig. 15, but with the frequency lower by 30%.

The avalanche can be avoided by stabilization of the $n = 5$ mode. In Fig. 19 is shown the evolution of the modes with a small increase in the damping of the mode $n = 5$ at $t = 25$ msec, just as the avalanche is about to take place.

An alternative way of inducing the mode explosion is by lowering the mode frequency. In Fig. 20 is shown a kinetic Poincaré plot of the $n = 5$ mode resonance, with the amplitude being the same as in Fig. 15, but with the mode frequency reduced by 30%, to 115 kHz. The resonances are significantly larger and there are more chaotic domains. The same is true of the other resonances. Thus, a decrease in the mode frequency, such as that seen occurring in Fig. 11, can also lead to an avalanche.

V. CONCLUSION

Two NSTX shots are considered, one with saturated Alfvén modes producing a small local modification of the high energy particle distribution and another producing an avalanche. Values of the mode growth rate and damping for the modes given by theoretical analysis are used. In the first case, an inspection of the resonances produced by the two modes present in the discharge shows them to be too few and too distant, not providing a path for significant particle stochastic loss, even at a large amplitude.

In the second case, the four modes observed are shown to produce resonances that can provide a path for large scale stochastic loss of particles with only a small increase in the high energy particle gradients producing the mode drive, or a decrease in the mode frequency. One particular mode is critical in providing a path for particle loss. If the mode drive is below this critical value, the mode amplitudes oscillate around saturation levels, which do not produce a significant modification of the high energy particle distribution away from the linear resonances. When the mode drive is increased or the frequency is reduced, the modes mutually destabilize one another, producing a strong avalanche and significant loss of fast ions. The analysis of the density and the nature of resonances connected with the unstable modes in the equilibrium provide an insight concerning the possibility of the avalanche, and can be used in a predictive manner. The avalanche can be avoided by stabilization of the $n = 5$ mode, principally responsible for providing a path for stochastic particle loss. We note, however, that the late stages of the avalanche crash MHD nonlinearities, not captured by the present study, likely play a principal role in the system dynamics.

ACKNOWLEDGMENTS

This work was supported by the U.S. Department of Energy (DOE) under Contract No. DE-AC02-09CH11466.

REFERENCES

- ¹S. M. Kaye, M. G. Bell, R. E. Bell, S. Bernabei, J. Bialek, T. Biewer, W. Blanchard, J. Boedo, C. Bush, M. D. Carter *et al.*, *Nucl. Fusion* **45**, S168–S180 (2005).
- ²E. Fredrickson, N. Gorelenkov, M. Podesta, A. Bortolon, S. Gerhardt, R. Bell, A. Diallo, and B. LeBlanc, *Nucl. Fusion* **54**, 093007 (2014).
- ³M. Podesta, R. E. Bell, A. Bortolon, N. A. Crocker, D. S. Darrow, A. Diallo, E. D. Fredrickson, G.-Y. Fu, N. N. Gorelenkov, and W. W. Heidbrink, *Nucl. Fusion* **52**, 094001 (2012).
- ⁴E. D. Fredrickson, N. A. Crocker, D. S. Darrow, N. Gorelenkov, G. Kramer, S. Kubota, M. Podesta, R. White, A. Bortolon, S. Gerhardt, R. E. Bell, R. Diallo, B. LeBlanc, F. Levinton, and H. Yuh, *Nucl. Fusion* **53**, 013006 (2013).

- ⁵K. Shinohara, Y. Kusama, M. Takechi, A. Morioka, M. Ishikawa, N. Oyama, K. Tobita, T. Ozeki, S. Takeji, S. Moriyama *et al.*, *Nucl. Fusion* **41**, 603 (2001).
- ⁶M. Ishikawa, M. Takechi, K. Shinohara, Y. Kusama, C. Z. Cheng, G. Matsunaga, Y. Todo, N. N. Gorelenkov, G. J. Kramer, R. Nazikian *et al.*, *Nucl. Fusion* **45**, 1474 (2005).
- ⁷H. L. Berk, B. N. Breizman, J. Fitzpatrick, and H. V. Wong, *Nucl. Fusion* **35**, 1661 (1995).
- ⁸R. B. White and M. S. Chance, *Phys. Fluids* **27**, 2455 (1984).
- ⁹N. N. Gorelenkov, C. Z. Cheng, and G. Y. Fu, *Phys. Plasmas* **6**, 2802 (1999).
- ¹⁰A. Pankin, D. McCune, R. Andre, G. Bateman, and A. Kritiz, *Comput. Phys. Commun.* **159**, 157 (2004).
- ¹¹R. B. White, N. Gorelenkov, M. Gorelenkova, M. Podesta, S. Ethier, and Y. Chen, *Plasma Phys. Controlled Fusion* **58**, 115007 (2016).
- ¹²M. Zhou and R. White, *Plasma Phys. Controlled Fusion* **58**, 125006 (2016).
- ¹³R. B. White, *The Theory of Toroidally Confined Plasmas*, 3rd ed. (Imperial College Press, 2014).
- ¹⁴Y. Chen, R. B. White, G.-Y. Fu, and R. Nazikian, *Phys. Plasmas* **6**, 226 (1999).
- ¹⁵A. N. Kolmogorov, in *Proceedings of the International Congress Mathematicians, Amsterdam (1957)*, Vol. 1, p 315; V. I. Arnold, *Russ. Math. Surv.* **18**(5), 9 (1963); J. Moser, *Math. Phys. Kl. II*(1), 1–20 (1962).
- ¹⁶V. N. Duarte, H. L. Berk, N. N. Gorelenkov, W. W. Heidbrink, G. J. Kramer, R. Nazikian, D. C. Pace, M. Podesta, B. J. Tobias, and M. A. Zeeland, *Nucl. Fusion* **57**(5), 054001 (2017).
- ¹⁷V. N. Duarte, N. N. Gorelenkov, M. Schneller, E. D. Fredrickson, M. Podesta, and H. L. Berk, *Nucl. Fusion* **58**(8), 082013 (2018).
- ¹⁸N. N. Gorelenkov and L. E. Zakharov, *Nucl. Fusion* **58**, 082031 (2018).
- ¹⁹N. N. Gorelenkov, H. L. Berk, and R. V. Budny, *Nucl. Fusion* **45**, 226 (2005).
- ²⁰V. N. Duarte and N. N. Gorelenkov, *Nucl. Fusion* **59**, 044003 (2019).
- ²¹X. Wang and S. Briguglio, *New J. Phys.* **18**, 085009 (2016).
- ²²R. B. White, *Commun. Nonlinear Sci. Numer. Simul.* **17**, 2200 (2012).
- ²³R. B. White, *Plasma Phys. Controlled Fusion* **53**, 085018 (2011).
- ²⁴M. Podesta, M. Gorelenkova, and R. B. White, *Plasma Phys. Controlled Fusion* **56**, 055003 (2014).
- ²⁵C. Z. Cheng and M. S. Chance, *J. Comput. Phys.* **71**, 124 (1987).
- ²⁶H. L. Berk, B. N. Breizman, and M. Pekker, *Phys. Rev. Lett.* **76**, 1256 (1996).
- ²⁷H. L. Berk, B. N. Breizman, J. Candy, M. Pekker, and N. V. Petviashvili, *Phys. Plasmas* **6**, 3102 (1999).
- ²⁸R. B. White, V. N. Duarte, N. N. Gorelenkov, E. D. Fredrickson, M. Podesta, and H. L. Berk, *Phys. Plasmas* **26**, 92103 (2019).
- ²⁹Y. Todo, *New J. Phys.* **18**, 115005 (2016).
- ³⁰A. Bierwage, K. Shinohara, Y. Todo, N. Aiba, M. Ishikawa, G. Matsunaga, M. Takechi, and M. Yagi, *Nucl. Fusion* **57**, 016036 (2017).
- ³¹A. Bierwage, K. Shinohara, Y. Todo, N. Aiba, M. Ishikawa, G. Matsunaga, M. Takechi, and M. Yagi, *Nat. Commun.* **9**, 3282 (2018).
- ³²P. Bak and C. Tang, *Phys. Rev. Lett.* **59**, 381 (1987).
- ³³P. Bak and C. Tang, *Phys. Rev. A* **38**, 364 (1988).